Acta Oceanol. Sin., 2020, Vol. 39, No. 3, P. 12–24
https://doi.org/10.1007/s13131-020-1565-5
http://www.hyxb.org.cn
E-mail: hyxbe@263.net

Effects of Kuroshio intrusion optimization on the simulation of mesoscale eddies in the northern South China Sea

Baoxin Feng[1], Hailong Liu[2, 3]*, Pengfei Lin[2]*

[1] College of Ocean and Meteorology, Guangdong Ocean University, Zhanjiang 524000, China

[2] State Key Laboratory of Numerical Modeling for Atmospheric Sciences and Geophysical Fluid Dynamics (LASG), Institute of Atmospheric Physics, Chinese Academy of Sciences, Beijing 100029, China

[3] College of Earth and Planetary Sciences, University of Chinese Academy of Sciences, Beijing 100049, China

Received 10 July 2019; accepted 10 October 2019

Abstract

The impacts of Kuroshio intrusion (KI) optimization on the simulation of meso-scale eddies (MEs) in the northern South China Sea (SCS) were investigated based on an eddy-resolving ocean general circulation model by comparing two numerical experiments with differences in their form and intensity of KI due to the optimizing topography at Luzon Strait (LS). We found that a reduced KI reduces ME activities in the northern SCS, which is similar to the observations. In this case, the biases of the model related to simulating the eddy kinetic energy (EKE) west of the LS and along the northern slope are remarkably attenuated. The reduced EKE modeling bias is associated with both the reduced number of anti-cyclonic eddies (AEs) and the reduced amplitude of cyclonic eddies (CEs). The EKE budget analysis further suggests that the optimization of the KI will change the EKE by changing the horizontal velocity shear and the slope of the thermocline, which are related to barotropic and baroclinic instabilities, respectively. The former plays the key role in regulating the EKE in the northern SCS due to the changing of the KI. The EKE advection caused by the KI is also important for the EKE budget to the west of the LS.

Key words: South China Sea, meso-scale eddy, Kuroshio intrusion, Luzon Strait

Citation: Feng Baoxin, Liu Hailong, Lin Pengfei. 2020. Effects of Kuroshio intrusion optimization on the simulation of mesoscale eddies in the northern South China Sea. Acta Oceanologica Sinica, 39(3): 12–24, doi: 10.1007/s13131-020-1565-5

1 Introduction

The South China Sea (SCS) is the largest semi-closed marginal sea in the Northwest Pacific. As in other regions, meso-scale eddies (MEs) are ubiquitous to the SCS based on both satellite observational (e.g., Wang et al., 2003; Lin et al., 2007; Liu et al., 2008; Chen et al., 2011) and model studies (e.g., Zhuang et al., 2010; Xiu et al., 2010; Yang et al., 2013; Lin et al., 2015; Sun et al., 2016; Feng et al., 2017). The northern SCS (defined as north of 15°N in the present study) is an eddy rich region, especially in the area west of the Luzon Strait (LS), extending to the eastern coast of Hainan Island along the continental shelf (Chen et al., 2011). This behavior is related to the influences of the monsoon, the complex regional topography and the Kuroshio intrusion (KI) (e.g., Wang et al., 2000). The other active eddy region in the SCS is located east of central Vietnam and is due to the coastal jets along the eastern coast of Vietnam in the summer season (Wang et al., 2006; Chen et al., 2012; Chu et al., 2017). Originally, MEs were studied by sporadic hydrographic data (e.g., Chu et al., 1998; Su et al., 1999). After the advent of satellite data, the number and properties of the MEs have been extensively studied (e.g., Wang et al., 2003; Chen et al., 2011). Recently, some in situ hydrographic data from specifically ME-targeted field campaigns were used to resolve the depth structures and dynamics of several MEs, with the addition of altimetry data (Zhang et al., 2013, 2016; Wang et al., 2015; Chen et al., 2015).

Because the in situ data are limited by their temporal and spatial resolution and the satellite data are limited for studying the vertical structures of the MEs, eddy-resolving ocean models have become important tools for studying MEs in recent years. The simulated MEs in the SCS have been systematically evaluated using a regional (Xiu et al., 2010) and a quasi-global ocean model (Feng et al., 2017). The models were also used to investigate the eddy shedding of the Kuroshio intrusion (Jia and Chassignet, 2011), the eddy energy sources and sinks (Yang et al., 2013), the three-dimensional features of the MEs (Lin et al., 2015), the Luzon Cold Eddy (He et al., 2015) and the interannual variabilities of eddy kinetic energy (EKE; Sun et al., 2016). However, the MEs in the models still share some common biases, such as smaller radii, longer lifetimes and larger amplitudes, compared to those found in the satellite data (e.g., Feng et al., 2017), albeit there are also uncertainties in the satellite data. The primary problem for most of these models is that they tend to overestimate the eddy activities in the northern SCS (Zhuang et al., 2010; Xiu et al., 2010; Lin et al., 2015; Sun et al., 2016; Feng et al., 2017); these activities are quantified via the EKEs, amplitudes and rotation speeds of the modeled MEs.

The eddy formation processes in the northern SCS are complex because of not only the influence of the local orographic wind jet (Qu, 2000; Pullen et al., 2008; Wang et al., 2008) and complex topography but also the presence of the Kuroshio intru-

Foundation item: The National Key R&D Program for Developing Basic Sciences under contract Nos 2016YFC1401401 and 2016YFC1401601; the National Natural Science Foundation of China under contract Nos 41576025, 41576026 and 41776030.
*Corresponding author, E-mail: lhl@lasg.iap.ac.cn; linpf@mail.iap.ac.cn

sion in the Luzon Strait (Wang et al., 2000; Li et al., 1998; Jia and Chassignet, 2011). The eddy shedding by the Kuroshio intrusion is considered an important source of eddy generation based on both the observational (Zhang et al., 2017) and model results (Jia and Chassignet, 2011). Nan et al. (2011) investigated the relationship between the Kuroshio path variations and eddy formation. In addition to causing eddy shedding in winter, this study also found that a change in the path of the Kuroshio intrusion in summer can drive the formation of a cyclonic eddy (CE) to its left and then cause an anti-cyclonic eddy (AE) further west. He et al. (2015) examined the effects of winds and the Kuroshio intrusion on long-lasting cold eddies, called the Luzon Cold Eddies (LCEs), using a local, zoomed, global model. These authors found that the Kuroshio intrusion can weaken the upper LCEs and enhance the lower layer LCEs. Sun et al. (2016) also found a strong correlation between the EKE in the northeastern SCS and the Luzon Strait transports (LSTs) on an interannual time scale: high EKEs corresponded to increased LSTs and vice versa. All previous works suggested that the Kuroshio intrusion had a strong correlation to the eddy activity to the west of the LS. Therefore, biases in modeling the Kuroshio intrusion may lead to biases in the predicted EKE or eddy activities in this region. Although scientists have found that many MEs, especially AEs, shed from Kuroshio intrusion during the past decades (Yuan et al., 2006; Wang et al., 2008; Jia and Liu, 2004; Zhang et al., 2013, 2016, 2017), studies of effect of Kuroshio intrusion on the properties of MEs in the northern SCS from the point view of model biases are rare.

The objective of this work is to investigate and understand the simulation of MEs after optimizing the KI in order to discuss the biases and improvements of the simulations. Therefore, in this study, a quasi-global, eddy-resolving ocean model (Yu et al., 2012; Liu et al., 2012; Zhou et al., 2014) was employed to examine the effect of KI optimization on the simulation of MEs in the northern SCS. Here, two experiments were conducted: a control experiment with a smoothed topography in the LS and a sensitivity experiment with a corrected topography in the LS to optimize the simulation of the KI. The form and intensity of the KI are significantly better simulated in the latter experiment. The effect of the islands in the LS on the KI was systematically examined by Huang et al. (2017). After a preliminary evaluation of the mean circulation in the northern SCS, the changes of the MEs simulated by the two runs were investigated in terms of their EKEs, the number of eddy generation and their amplitudes, as well as other properties to investigate the improvements of the simulation of MEs, in both winter and summer. We also conducted diagnostic analyses of changes in the EKE budget between the two runs to improve our understanding of the dynamics behind these changes.

The paper is organized as follows. The model and experiments are described in Section 2. Section 3 introduces the eddy detection and tracking methods. The results of the two numerical experiments are presented in Section 4. The results are explained via the EKE budget due to eddy-mean flow interactions in Section 5. The findings of this study are summarized in Section 6.

2 Model and experiments

The results of a quasi-global eddy-resolving ocean general circulation model, specifically the State Key Laboratory of Numerical Modeling for Atmospheric Sciences and Geophysical Fluid Dynamics/Institute of Atmospheric Physics (LASG/IAP) Climate System Ocean Model version 2.0 (LICOM2.0) (Liu et al., 2012), are used in the present study. Several updates and improvements have been implemented in the eddy-resolving version of this model. To avoid the singularity of the North Pole in the longitude–latitude grid, the model domain covers only 66°N–79°S with an eddy-resolving horizontal resolution of 0.1° for both latitude and longitude. The number of vertical layers is increased to 55 layers. Thirty-six uneven layers are present in the upper 300 m, with a mean thickness of less than 10 m. In addition, biharmonic viscosity and diffusivity schemes are used in the momentum and tracer equations, respectively. The parameterization of eddies from Gent and McWilliams (1990) is also turned off in the tracer equations. Moreover, the parallel domain partitioning is changed to a two-dimensional method, including both zonal and meridional splitting.

The eddy-resolving model was initialized with observed temperature and salinity measurements (WOA09) and was then integrated over 12 a, starting at zero velocity and forced by the climatological monthly wind stresses and heat fluxes from the Ocean Model Intercomparison Project (OMIP; Roeske, 2001). After the 12-year spin-up experiment, the model was integrated over 60 years, beginning at the end of the 12th year of spin-up integration. For this 60-year period, the model was forced by the daily Coordinated Ocean-Ice Reference Experiments (COREs) algorithm and data from 1948 to 2007 (Large and Yeager, 2004). Owing to the lack of a sea ice module in LICOM2.0, the sea ice concentration was derived from the observational dataset from the Hadley Center (HadISST) (https://climatedataguide.ucar.edu/climate-data/sea-ice-concentration-data-hadisst).

The topography of LICOM2.0 is derived from the Digital Bathymetric Data Base 5 min (DBDB5) from the Naval Oceanographic Office and was heavily smoothed to guarantee the numerical stability. Therefore, the topography within the LS is not well modeled, as it misses some islands and the deep-water passage, as shown in Figs 1b and c. Based on the LICOM2.0, which has coarse topography in the Luzon Strait, Feng et al. (2017) found large discrepancies of eddy basic properties between satellite and model in the northern SCS due to the stronger Kuroshio intrusion. Metzger and Hurlburt (2001) found the small islands at the Luzon Strait can cause a reduction in the modeled westward intrusion of the Kuroshio into the SCS. Thus, according to the ETOPO2 dataset and navigation chart, we manually corrected the topography in the Luzon Strait by correcting the island chains, switching on the deep-water passage and modifying the depth of an important sill (Fig. 1d). The corrected topography is identical to that of Exp5 in Huang et al. (2017). An 18-year (1990–2007) sensitivity experiment was conducted using the corrected topography and the same forcing data as the control run. The daily outputs between 1993 and 2007 from the two experiments are used in this study. For convenience, we defined the control and the sensitivity experiments as ExpA and ExpB hereafter, respectively.

3 Eddy detection method, tracking method and satellite data

The eddy detection method used in this paper is the WA method (Chaigneau et al., 2009), which has been widely applied in the SCS (Chen et al., 2011; Feng et al., 2017), the Atlantic Ocean (Chaigneau et al., 2009) and the broader global oceans (Chelton et al., 2011). First, we identify possible CE (or AE) centers by searching for local SLA minima (or maxima) in a moving window of 1°×1° grid points. Then, for each possible CE (or AE) center, the algorithm searches for closed contours with an increment (or decrement) of 1 mm. The outermost closed SLA contour that encloses only the chosen center is considered the eddy edge. Following previous studies (e.g., Chaigneau et al., 2009;

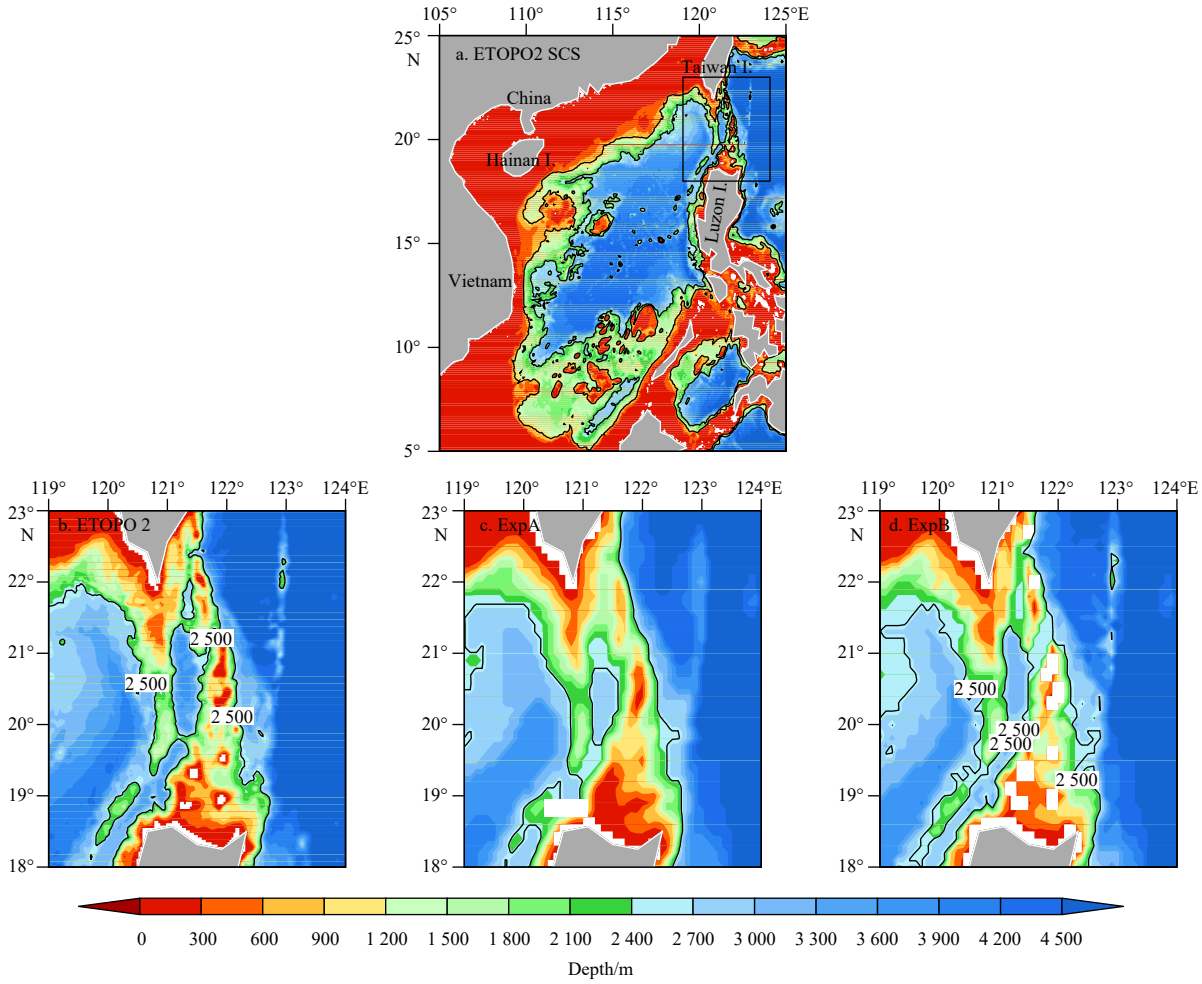

Fig. 1. The topography of the SCS (a) and the area around the Luzon Strait for ETOPO2 (b), ExpA (c) and ExpB (d). Unit: m.

Chen et al., 2011), we focus on eddies with amplitudes greater than 3 cm, lifetimes greater than five weeks, and depths greater than 200 m. The eddy tracking method used in this paper is based on the geometrical distance from one eddy center to another (e.g., Isern-Fontanet et al., 2003, 2006). The MATLAB code for this method was obtained from Lin et al. (2007) and was slightly modified. We have modified the minimum strength requirement for eddy detection, from 8 cm in the work of Lin et al. (2007) to 3 cm in this paper. Because we focus on eddies with amplitude greater than 3 cm, following previous studies (e.g., Chaigneau et al., 2009; Chen et al., 2011; Feng et al., 2017)

When we find the eddy centers and edges, some basic eddy properties can be estimated. Then, we can define the eddy amplitude as the absolute difference in the SLA between the eddy centers and the eddy edges. We can further define the eddy rotation speed, U, as the mean of the average geostrophic speeds inside the closed contours. The moving speed of the eddy, c, can be calculated by determining the distance moved over a time interval from the results of the eddy tracking. Following Chelton et al. (2011), we define the nonlinear parameter as U divided by c.

The satellite data used in this study are a gridded merged product of the Maps of Sea Level Anomaly (MSLA) and the Absolute Dynamic Topography (MADT) from 1993 to 2007, which was produced and distributed by AVISO (http://www.aviso.oceanobs.com/) based on data from TOPEX/Poseidon, Jason 1, ERS-1, and ERS-2 (Ducet et al., 2000). The spatial resolution of the satellite data is 0.25°×0.25°,and the temporal interval is seven days. Then, to make the model and satellite data consistent, the SSHA data from the model are interpolated onto the same 0.25°×0.25° grid, and the data are selected on seven-day intervals.

4 Results

4.1 *The Kuroshio intrusion and circulation in northern SCS*

Figure 2 shows the surface geostrophic circulations in the boreal winter (December–January–February, i.e., DJF) and summer (June–July–August, i.e., JJA) in the northern SCS from the altimeter observation, ExpA and ExpB results, respectively. The shading is the sea surface height anomaly (SSHA) minus the SCS basin mean values. The northern SCS is defined as 15°–25°N, and 105°–121°E hereafter. Because of both the monsoon and the KI, the basin circulation in the upper layer of the SCS is cyclonic in winter, and in summer, it is cyclonic in the northern half of the basin and anticyclonic in the southern half (Qu, 2000). These patterns can be found in the surface geostrophic currents and the SSHAs of the observations (Figs 2a and d). However, in the control run, ExpA, the model severely overestimates the surface circulation in the northern SCS. Both the magnitude of the currents and the gradients of the SSHA found in the results of ExpA are larger than those in the satellite observations. The patterns of the circulations seen during JJA in ExpA obviously differ from those found in the observational data. Due to the strong KI in summer,

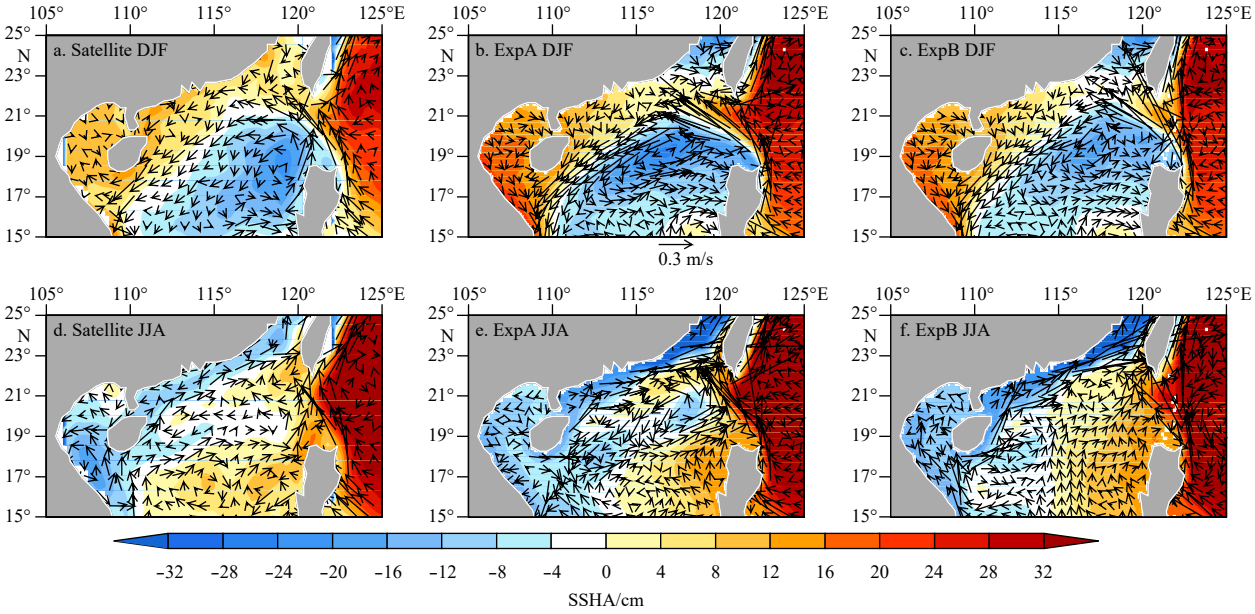

Fig. 2. The winter (DJF, a, b, c) and summer (JJA, d, e, f) mean upper layer geostrophic circulation (vector) and sea surface height anomaly (shaded) for the satellite, ExpA and ExpB data in the northern SCS, respectively. The mean values of the sea surface height anomaly in the SCS basin have been subtracted. Units: m/s and cm.

there is a strong recirculation collocated with a low SSHA just west of the LS in ExpA (Fig. 2e), which is not found in the observational data.

There are significant differences between the surface circulations found by the two experiments. The form and intensity of the KI simulated in ExpB is more similar to that observed in satellite compared with ExpA, although it is still stronger. In winter, the KI and the southwestward flow along the shelf for ExpB are still stronger than those of the observational dataset, but both are much weaker than those of ExpA. The magnitude of the minimum SSHA in ExpB is also close to the satellite data, though it is located further west. In summer, ExpB has a magnitude of the KI similar to that found by the satellite, and the patterns of the SSHA and surface currents are also similar to those found by the satellite. There is no center for the low values of SSHA west of the LS in ExpB. These changes in the surface currents lead to decreases in the horizontal shear of the velocity in the northern SCS: both anti-cyclonic and cyclonic occur west of the LS during DJF, with cyclonic along the shelf in the same period, and cyclonic also occur both west of the LS and along the shelf during JJA. These differences between the model and observational data suggest that there may also be a difference in the ratio of the modeled anticyclonic eddies (AEs) and cyclonic eddies (CEs), which is examined in the following analysis.

The comparisons between ExpB and the observational data show some clear differences. As noted above, ExpB still overestimates surface currents and the western low value center of SSHA during DJF. This overestimation may be related to other characteristics of the model, including the uncertainties in the forcing datasets and the subgrid parameterizations of the model, in addition to the topography in the LS. However, here, we seek to understand the differences between two experiments, especially the changes in the MEs after optimizing the KI, not the differences between the simulations and the observational data. Therefore, the biases in the original model are acceptable for our purposes.

4.2 *Eddy kinetic energy*

Before we analyze the properties of the MEs, we investigate the eddy kinetic energy (EKE) in the satellite, ExpA and ExpB data (Fig. 3). The EKE are all computed as follows:

$$\mathrm{EKE} = \frac{1}{2}\left(u'^2 + v'^2\right),$$

where u' and v' are the geostrophic velocity anomalies deduced from the SLA maps using the geographic approximations, $u' = -\frac{g}{f}\frac{\partial\,(\mathrm{SLA})}{\partial y}$ and $v' = \frac{g}{f}\frac{\partial\,(\mathrm{SLA})}{\partial x}$, where g (=9.8 m/s^2) is the gravitational constant and f is the Coriolis parameter. In the observational data, high EKE occurs west of the Luzon Strait, along the northern slope and east of Vietnam. For convenience, we defined the west of the Luzon Strait (18.5°–22.5°N, 117.5°–121.5°E) and along the northern slope (16.5°–19.5°N, 112.5°–116.5°E), which we mainly focus on in this paper, as A1 and A2 hereafter, respectively. There are also distinct seasonal variabilities, especially in the A1 and east of Vietnam regions: EKE is large in winter and small in summer for A1, which is related to the magnitude of the KI and local wind stresses, and the seasonal variability of EKE is opposite in the east of Vietnam region.

In general, the model can well reproduce the spatial patterns and the seasonality of the EKE, but both ExpA and ExpB simulate a higher amplitude EKE than that seen in the satellite data for all of the three regions. When the KI is optimized in ExpB, the EKE in the A1 and A2 regions are less than those in ExpA, which is more similar to the observations. The most evident reduction of EKE occurs in the A1 region during the winter season. Therefore, we will now focus on the A1 and A2 regions, which are represented by the two boxes in Fig. 3 (A1 (18.5°–22.5°N, 117.5°–121.5°E) and A2 (16.5°–19.5°N, 112.5°–116.5°E)). The area-averaged EKEs for A1 in ExpB are approximately 44% and 17% smaller than those in ExpA during winter and summer, respectively, and are reduced by approximately 37% and 27% for A2 region. In a word, the distribution and magnitude of EKE simulated by Ex-

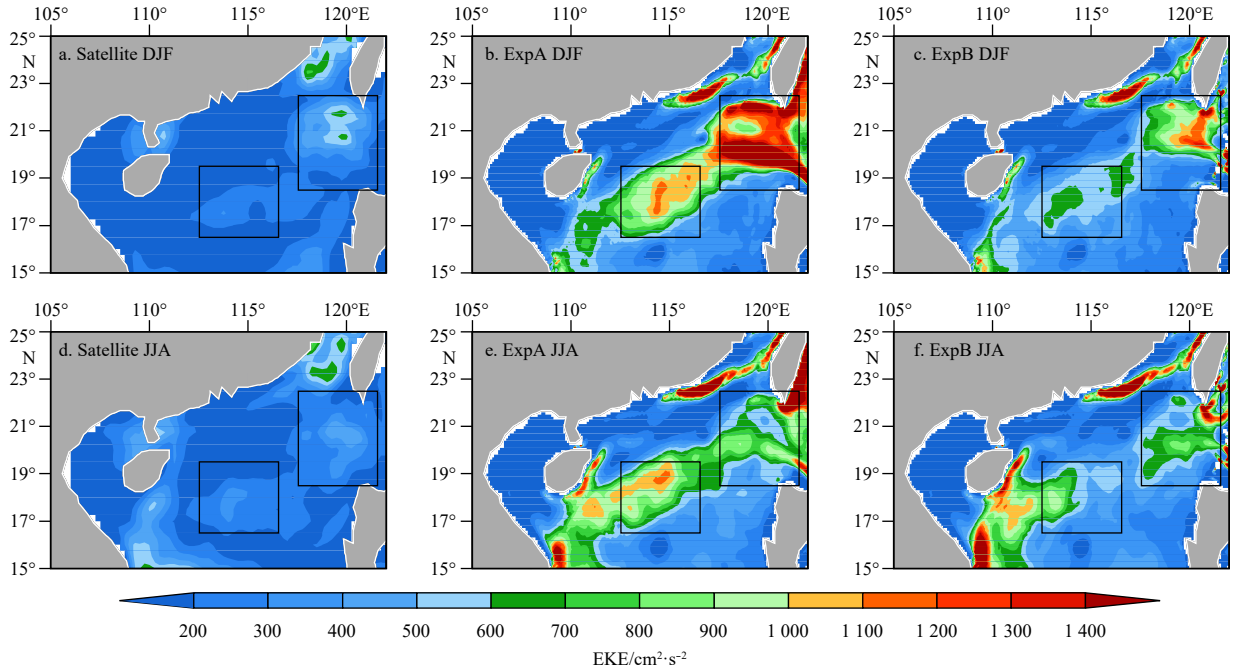

Fig. 3. The winter (DJF, a, b, c) and summer (JJA, d, e, f) mean EKE for the satellite, ExpA and ExpB data, respectively. The two boxes are the regions we focus on in the present study: the region west of Luzon Strait (A1, 18.5°–22.5°N, 117.5°–121.5°E) and the North Shelf (A2,16.5°–19.5°N, 112.5°–116.5°E). Unit: cm^2/s^2.

pB becomes more similar to that observed in satellite, when we optimized the form and intensity of KI in ExpB.

The differences in the mean flow and the EKE between the two experiments suggest that changes of the Kuroshio intrusion, which is optimized in ExpB, can affect the ME activities in the northern SCS region. Since EKE is related to both the number and magnitudes of the MEs, changes in both the numbers and amplitudes of the MEs are investigated in the following two subsections, respectively.

4.3 *Number of eddies*

In the northern SCS, 326 eddies are detected during the period of 1993–2007, using satellite altimeter data (Table 1). The numbers of CE and AE are almost the same, with 164 CEs and 162 AEs. The number of eddy generation for ExpA is approximately 34% larger than that of the observation total, with 41% more CEs and 27% more AEs. There are fewer eddies generated in ExpB, which partly contributes to the reduced EKE in the northern SCS. After modifying the LS and optimizing the KI (ExpB), the number of eddies created in the northern SCS decreases by approximately 10%, such that it is only 24% larger than that observed. Note that the number of CEs simulated by ExpB does not change much (with a decrease of only 4%). The number of AEs created in ExpB decreases by approximately 17%.

To investigate the spatial patterns of the changes in the number of eddies, we investigated the spatial patterns of the number of AEs, which is significantly decreased in ExpB. Figure 4 shows the total number of AEs in each 1°×1° grid according to satellite observations, ExpA and ExpB for two seasons. In the observational data, the largest number of AEs can be found in the A1 region during both winter and summer. AEs in winter are related to the looping pattern of the KI (Fig. 2a), while AEs in summer are related to CEs associated with the leaping path of the Kuroshio (Fig. 2d, Nan et al., 2011). In the A2 region, AEs mainly occur in the summer season and are driven by the eastward currents along 18°N (Fig. 2d).

There are significantly more AEs in ExpA for both regions and both seasons, which may be due to the extremely strong KI and along-shelf currents (Figs 2b and e). In ExpB, the significant reductions in the KI and the surface currents lead to a reduction of AEs in both regions, especially during winter, when the KI is strongest. Table 2 shows the number of AEs in winter and summer detected based on satellite, ExpA and ExpB data in the A1 and A2 regions. In the A1 region, the number of eddies is reduced from 22 for ExpA to 18 for ExpB, and in the A2 region, the count drops from 13 for ExpA to 9 for ExpB. The observational data showed over 40% fewer eddies than either of the model results. These results are consistent with the analysis of EKE in the previous subsection.

Table 1. The number of CEs and AEs observed in satellite, ExpA and ExpB data in the northern SCS (16°–24°N, 105°–121.5°E)

Region	Data	Total	CE	AE
Northern SCS	Satellte	326	164	162
	ExpA	436(34%)	231(41%)	205(27%)
	ExpB	404(24%)	225(37%)	179(10%)

Note: The numbers in the parentheses are the relative changes of model results compared to the observational data.

4.4 *Amplitude and other properties of eddy*

In addition to the number of eddies, the magnitude of the eddies also contributes to the EKE. Here, we use the amplitudes of eddies to measure their magnitudes. This amplitude is defined as the sea surface anomaly between the center and the outside edge of each eddy. The mean values of the amplitudes and other properties of the eddies are shown in Table 3, including radii, lifetimes, moving speeds, rotation speeds and their nonlinear parameters. In the observational data, the mean amplitudes for the

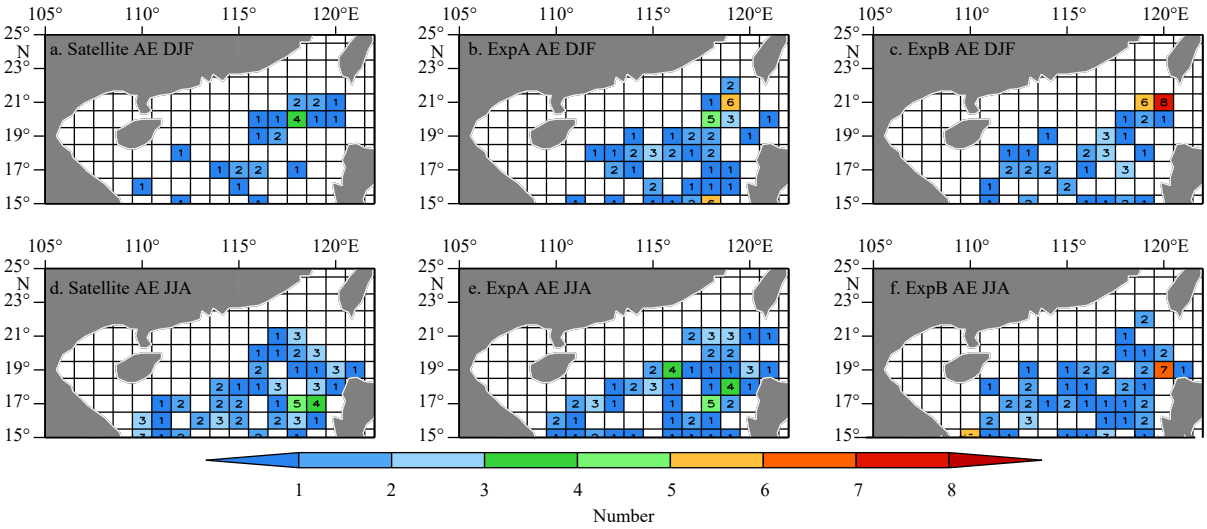

Fig. 4. The number of AEs observed in satellite data (a, d), ExpA (b, e) and ExpB (c, f) in winter (DJF) and summer (JJA) during 1993–2007. The values are computed for a 1°×1° grid

Table 2. The number of AEs observed in the satellite, ExpA and ExpB data in the A1 (18.5°–22.5°N, 117.5°–121.5°E) and A2 (16.5°–19.5°N, 112.5°–116.5°E) regions.

Region	Data	DJF	JJA
A1	Satellte	11	14
	ExpA	22 (100%)	18 (29%)
	ExpB	18 (64%)	17 (21%)
A2	Satellte	6	10
	ExpA	13 (117%)	15 (50%)
	ExpB	9 (50%)	14 (40%)

Note: The numbers in the parentheses are the relative changes of model results compared to the observational data.

Table 3. The statistical properties of the CEs and AEs for the satellite, ExpA and ExpB data in the northern SCS

Variables	Eddy	Satellite	ExpA	ExpB
Amplitude/cm	CE	14.9	22.1(48%)	18.1(21%)
	AE	17.2	22.2(29%)	20.7(20%)
Radius/km	CE	151.2	138.8(–8%)	138.0(–9%)
	AE	176.3	158.9(–10%)	150.7(–15%)
Lifetime/week	CE	7.9	9.9(25%)	9.7(23%)
	AE	7.6	8.3(9%)	8.7(14%)
Moving speed (c)/cm·s^{-1}	CE	5.4	5.8(7%)	6.2(15%)
	AE	5.4	6.0(11%)	6.1(13%)
Rotation speed (U)/cm·s^{-1}	CE	18.9	27.5(46%)	24.4(29%)
	AE	18.7	27.3(46%)	25.9(39%)
Nonlinear parameter (U/c)	CE	3.9	5.4(38%)	4.3(10%)
	AE	3.9	4.9(26%)	4.6(18%)

Note: The numbers in the parentheses are the relative changes of model results compared to the observational data.

CEs and AEs are 14.9 cm and 17.2 cm, respectively. The simulated eddies in ExpA are much stronger than those in the satellite data. The mean amplitudes of the CEs and AEs for ExpA are both approximately 22 cm, which are approximately 48% and 29% larger than those from the satellite data. However, in ExpB, the amplitudes of the eddies are significantly reduced and are only 21% larger than the satellite data for the CEs and 20% larger for the AEs, which is more similar to that of satellite data compared with ExpA.

To investigate the spatial patterns of the eddy amplitudes, the average amplitude for all CEs and AEs in each 1° × 1° region for both seasons are shown in Figs 5 and 6. In winter, the strong CEs (larger than 17 cm) found in the satellite data mainly occur south of 18°N, with only a small number of strong CEs appearing in the A1 region (Fig. 5a). However, there is a belt of strong AEs beginning at the A1 and extending southwest along the shelf to the southeast of the Hainan Island (Fig. 5d). The centers of the large values appear in the A1 and A2 regions. As previously mentioned, strong AEs are closely related to the looping shape of the KI and the eddies shed in winter. The overestimated KI and along-shelf currents in ExpA lead to a belt of strong eddies in the northern SCS, largely composed of CEs, which can extend all the way to the coast of Vietnam with values of more than 25 cm (Figs 5b and e). The spatial pattern of the AEs is like those seen in the observational data. The magnitudes of the CEs are greatly reduced in ExpB, while the magnitudes of the AEs are hardly changed (Figs 5c and f). The magnitudes of the eddies in ExpB in winter are reduced by approximately 20% in both the A1 and A2 regions (Tables 4 and 5). Note that a small increase in the AEs near the coast of Vietnam occurs. This increase will not be discussed further in this study.

In summer, the magnitudes of eddies in the A1 are weakened, while the strong AEs related to the coastal currents along Vietnam become significant. ExpA overestimates both the CEs and AEs in the northern SCS, while the CEs are relatively reduced in ExpB. The magnitudes of eddies in ExpB are reduced by approximately 14% and 8% in the A1 and A2 regions, respectively (Tables 4 and 5). Briefly, after optimizing the KI simulated by ExpB, the spatial distribution and magnitude of MEs in ExpB is more similar to that of satellite data compared with ExpA.

We also investigated other properties of the eddies, such as their radii, the lifetimes, moving speeds, rotation speeds and nonlinear parameters. The model tends to simulate strong, small and fast moving eddies, as we summarized in our previous paper (Feng et al., 2017). It also tends to simulate longer lifetimes and stronger nonlinearities than seen in the observational data (Table 2). When the topography of the LS is modified and the bias in the KI model is reduced, the rotation speeds and the nonlinear parameter values, which are closely related to the amplitude of an eddy, are also decreased. However, other properties, such

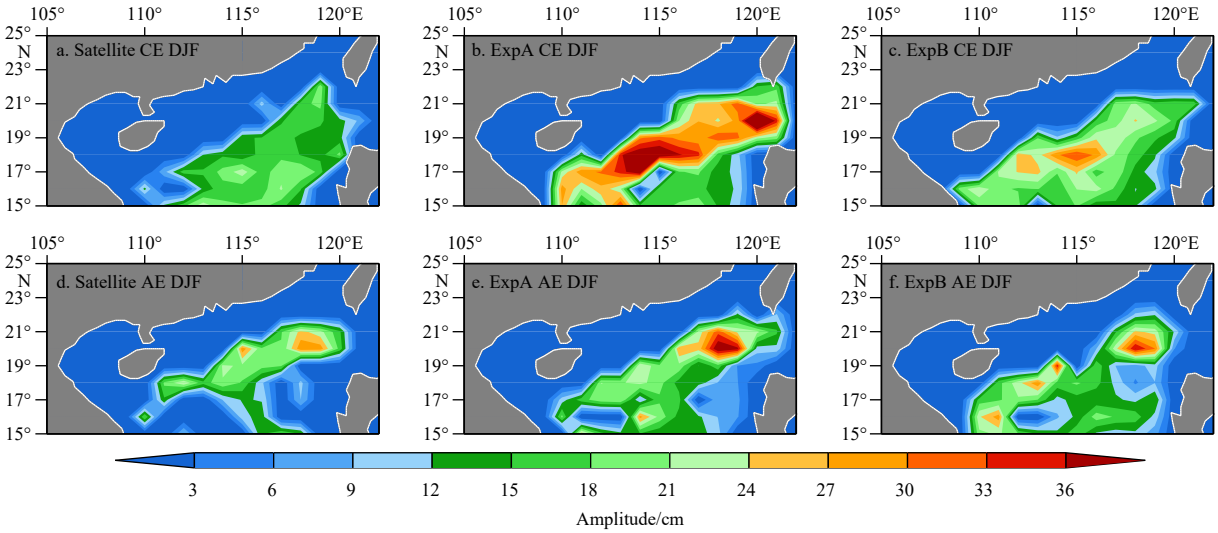

Fig. 5. The average amplitudes of the CEs and AEs observed by satellite (a, d), ExpA (b, e) and ExpB data (c, f) in winter (DJF). The values are averaged across a 1°×1° grid. Unit: cm.

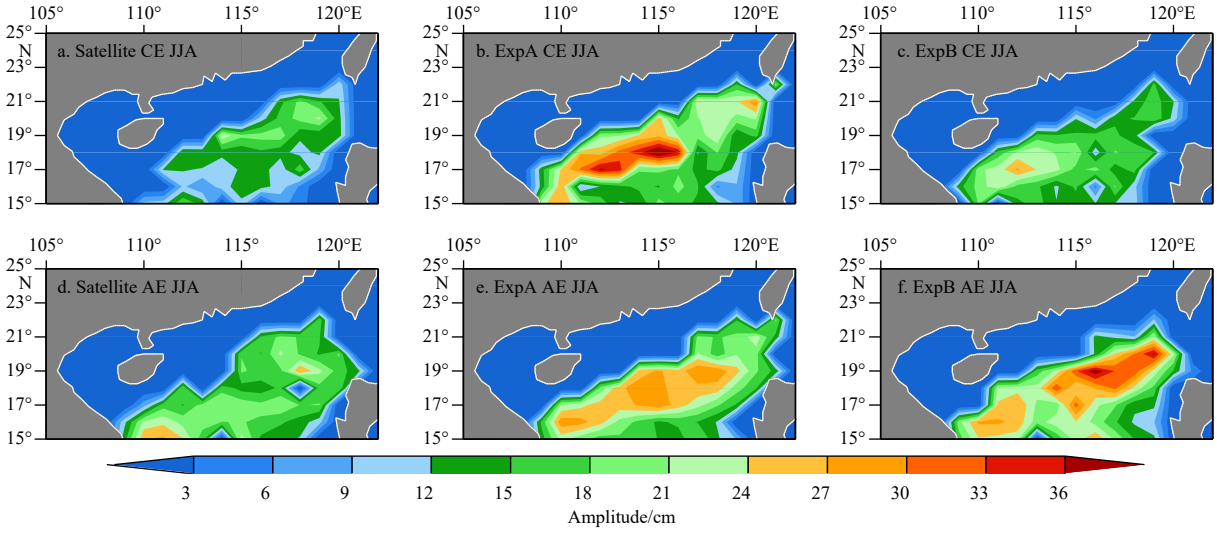

Fig. 6. The average amplitudes of the CEs and AEs observed by satellite (a, d), ExpA (b, e) and ExpB data (c, f) in summer (JJA). The values are averaged across a 1°×1° grid. Unit: cm.

Table 4. The area average of EKE, amplitude, D_{K_E}, M_{K_E}, and A_{K_E} in DJF and JJA in the A1 region (18.5°–22.5°N, 117.5°–121.5°E) for ExpA and ExpB

Season	Experiment	EKE/cm^2·s^{-2}	Amplitude/cm	D_{K_E}/mW·m^{-2}	M_{K_E}/mW·m^{-2}	A_{K_E}/mW·m^{-2}	Sum of the budget terms/mW·m^{-2}
DJF	ExpA	1 108.5	21.7	1.1	2.1	3.6	6.8
	ExpB	626.2(–44%)	16.9(–22%)	0.8(–30%)	1.8(–14%)	1.4(–61%)	3.0
JJA	ExpA	663.3	20.1	0.3	2.4	1.1	3.8
	ExpB	552.3 (–17%)	17.2 (–14%)	0.2 (–33%)	1.2 (–50%)	0.5 (–55%)	1.9

Table 5. The area average of EKE, amplitude, D_{K_E}, M_{K_E}, and A_{K_E} in DJF and JJA in the A2 region (16.5°–19.5°N, 112.5°–116.5°E) for ExpA and ExpB

Season	Experiment	EKE/cm^2·s^{-2}	Amplitude/cm	D_{K_E}/mW·m^{-2}	M_{K_E}/mW·m^{-2}	A_{K_E}/mW·m^{-2}	Sum of the budget terms/mW·m^{-2}
DJF	ExpA	814.6	25.8	0.7	5.3	4.7	10.7
	ExpB	513.6(–37%)	21.0(–19%)	0.5(–29%)	2.1(-60%)	3.0(–36%)	5.6
JJA	ExpA	726.8	23.6	0.6	3.9	0.8	5.3
	ExpB	531.2(–27%)	21.6(–8%)	0.3(–50%)	1.5(–62%)	1.4(75%)	3.2

the radii, the lifetimes and the moving speeds, do not change significantly.

The previously stated analysis of the number and the amplitudes of eddies suggested that the decrease in EKE in the A1 and A2 regions for ExpB due to the KI optimization are primarily related to a reduction in the number of AEs in winter and a reduction in the magnitude of the CEs in both seasons. We also investigated the change in the number of CEs seen in each experiment. However, we found that the number of CEs in ExpB is even slightly increased in the two study regions (not shown). Therefore, we propose that the changes in the magnitudes of the MEs may be a more significant factor to the changes of EKE. In the following section, we will attempt to explain the reduced EKE using the diagnostic framework of the EKE budget proposed by Chen et al. (2014). This approach will help us understand the physical processes behind the reduction of EKE in ExpB.

5 EKE budget

In Chen et al. (2014), the prognostic equation of EKE can be written as follows:

$$\frac{\partial K_E}{\partial t} + \nabla \cdot \left[\vec{u}\frac{1}{2}\rho_0\left(\overline{u'^2 + v'^2}\right)\right] + \nabla \cdot \left(\overrightarrow{\overline{u'p'}}\right) = -g\overline{\rho' w'} - \rho_0\left(\overrightarrow{\overline{u'u'}} \cdot \nabla\bar{u} + \overrightarrow{\overline{v'u'}} \cdot \nabla\bar{v}\right) + \rho_0\left(\overline{u'D_u'} + \overline{v'D_v'}\right),$$

where the overbar (–) and prime (′) denote the time average and the anomaly. K_E is the time averaged eddy kinetic energy, which is calculated by $K_E = \frac{1}{2}\rho_0\left(\overline{u'^2 + v'^2}\right)$, where u, v and w are the velocities in three directions, respectively. p is the pressure, ρ_0 (= 1 030 kg/m^3) is the density of seawater, and D_u and D_v stand for the rates of the momentum change due to the horizontal viscosity in the x and y directions. The vectors $\vec{u}$ and $\overrightarrow{u'}$ are the three-dimensional velocity vector and the scalars u, v, u' and v' are the velocity or velocity anomaly in the x and y directions, respectively. The three terms on the left-hand side of the equation are the tendency of the EKE and the redistribution of the EKE due to horizontal advection and due to pressure work. The negative redistribution of the EKE due to horizontal advection is denoted as A_{K_E} hereafter. The terms on the right-hand side represent the amount of EKE gained from the eddy potential available energy (EAPE), which we define as D_{K_E} hereafter; the change of EKE due to fluxes in eddy momentum is defined as M_{K_E} hereafter; and the dissipation term, which accounts for the amount of EKE lost due to friction, wind stress and bottom drag. In this study, we focus on D_{K_E}, M_{K_E} and A_{K_E}, which measure the energy the eddies gained from the mean flow due to the EAPE released, the fluxes in eddy momentum, and the energy transported by both the mean and eddy flows. These terms are the three primary ways that the mean currents affect the EKE, and are the dominant terms of the EKE budget. The first two terms are usually believed to relate to baroclinic and barotropic instabilities.

The upper 200 m of integrated D_{K_E}, M_{K_E} and A_{K_E} for the two experiments are shown in Figs 7, 8 and 9, respectively. The positive (negative) values mean a gain (loss) of EKE due to these three processes. It is obvious that the spatial patterns of the three terms are related to the mean flow (Fig. 2). The large positive and negative values of the three terms can also be found in the A1 and A2 regions, where the surface currents are strong due to the KI and along-shelf currents, respectively. For ExpA, M_{K_E} dominates the EKE budget of the two areas, but the contributions from the other two terms cannot be neglected. The relationship between M_{K_E} and D_{K_E} in the present study is similar to that seen in the western part of the western boundary extension regions examined in Chen et al. (2014). The D_{K_E} and M_{K_E} have similar patterns, while

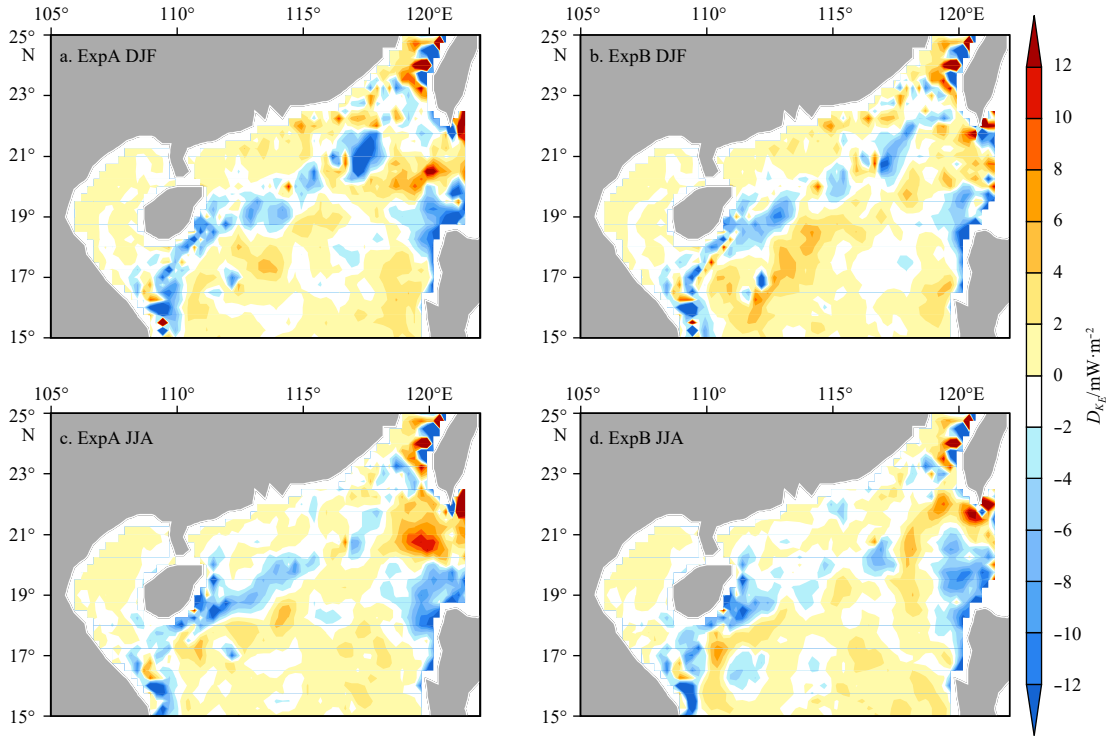

Fig. 7. The upper 200 m integrated D_{K_E} for ExpA in the DJF (a) and JJA seasons (c) . (b, d) is the same as (a, c), but for ExpB. Unit: mW/m^2.

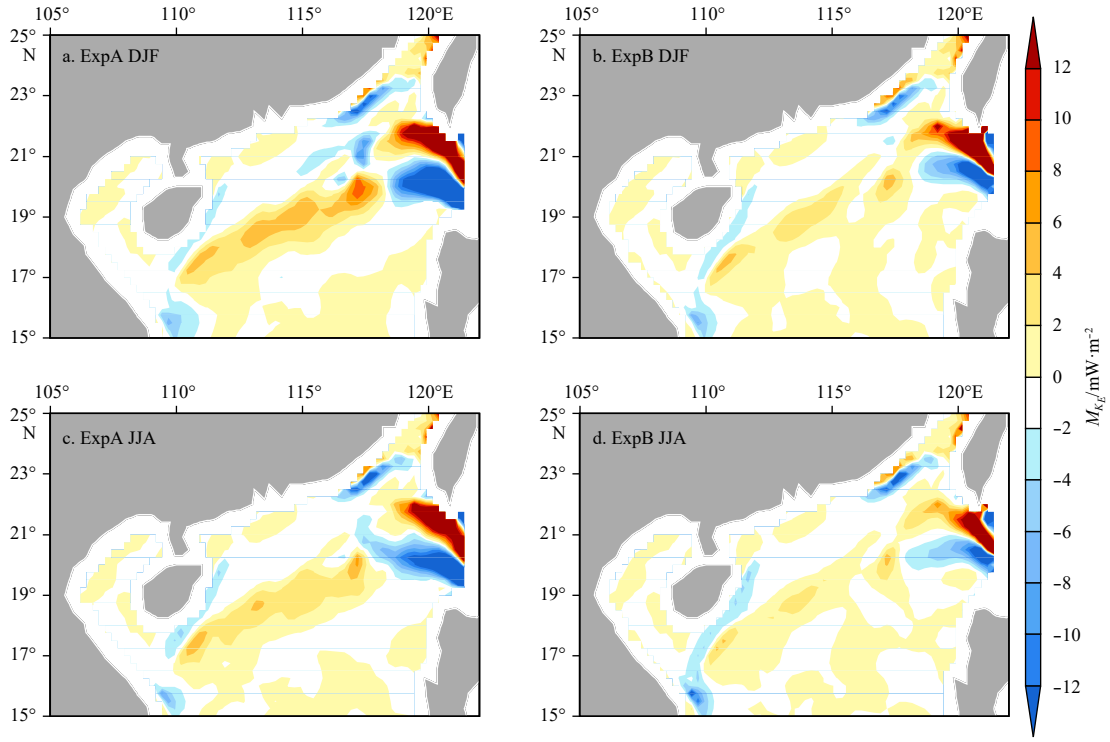

Fig. 8. The upper 200 m integrated M_{K_E} for ExpA in the DJF (a) and JJA (c) seasons. (b, d) is the same as (a, c), but for ExpB. Unit: mW/m^2.

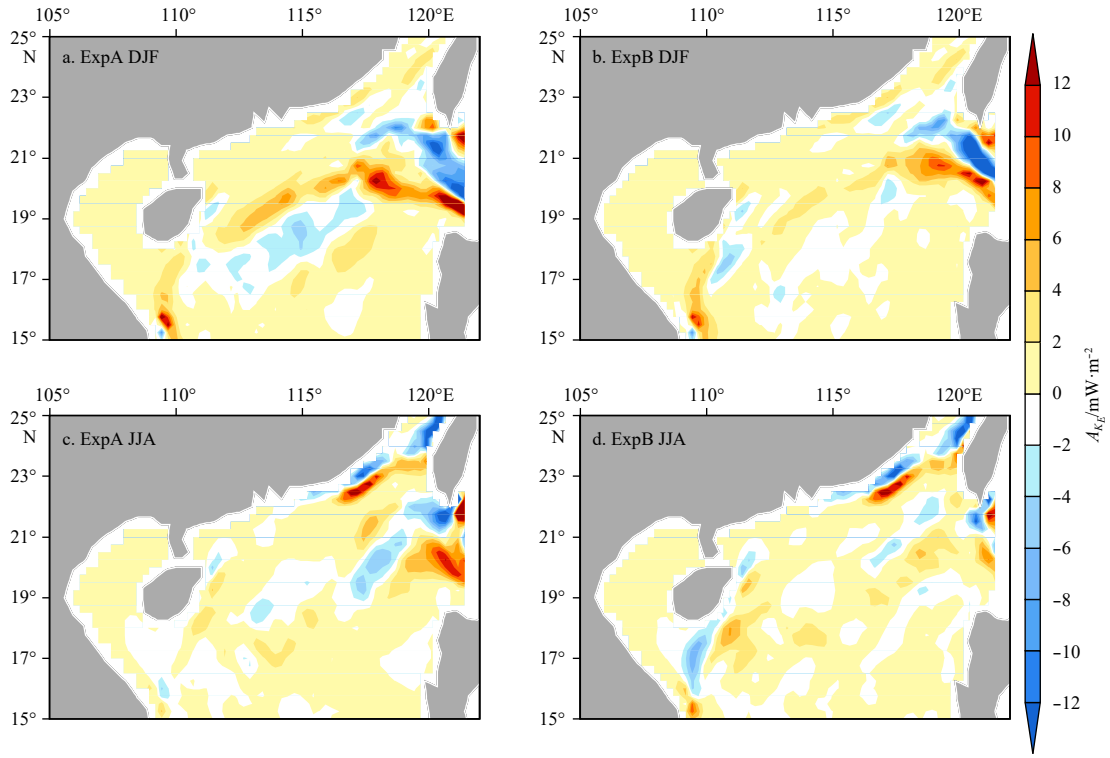

Fig. 9. The upper 200 m integrated A_{K_E} for ExpA in the DJF (a) and JJA(c) seasons . (b, d) is the same as (a, c), but for ExpB. Unit: mW/m^2.

the values of A_{K_E} and M_{K_E} are mostly opposite. This finding indicates that the transfer of EKE from the fluxes in eddy momentum or from the EAPE releases is canceled out by the horizontal transport of the EKE. For ExpB, the magnitudes of all three terms are significantly reduced, while the spatial patterns do not change much, apart from A_{K_E} in A1 during summer, where the large values almost disappear. Interestingly, the magnitudes of A_{K_E} along the east coast of Vietnam are slightly increased during JJA. This

increase may be linked to the increase in EKE in this area.

To analyze these three terms more quantitatively, we computed the area-averaged and upper 200 m integrated D_{K_E}, M_{K_E} and A_{K_E} for the A1 and A2 regions (Tables 4 and 5). We first focus on the A1 region, where the M_{K_E} and A_{K_E} terms are larger than D_{K_E}. During winter, the eddy energy gained from D_{K_E}, M_{K_E} and A_{K_E} in ExpA is 1.1, 2.1 and 3.6 mW/m^2, respectively, but the values decreased to 0.8, 1.8 and 0.3 mW/m^2, respectively, for ExpB, which decreased approximately 30%, 14% and 92%, respectively. In summer, D_{K_E} for ExpA decreases to 0.3 mW/m^2. That is, the contribution of energy transport from the EAPE is reduced due to a decrease in the KI (Figs 2c and f). However, in ExpB, all of the three terms are decreased by more than 25% in summer. Comparing between the two experiments, we found that all three of the terms contribute to the decrease in EKE but that A_{K_E} dominates the winter budget, while M_{K_E} and A_{K_E} dominate summer. Considering the seasonal variability of EKE, D_{K_E} and A_{K_E} is dominant in both ExpA and ExpB. The enhanced D_{K_E} in winter means that the baroclinic instabilities become stronger, which is consistent with the results of Chen et al. (2012), that the baroclinic instability enhanced the EKE in A1 in winter. The seasonal variability of A_{K_E} is related to the seasonal variability of Kuroshio intrusion. As mentioned above, the reduction of the KI not only decreases the magnitude of the surface currents in the northern SCS but also decreases the magnitude of the horizontal velocity shear. The former leads to less EKE being transported by the Kuroshio intrusion in the A1 region, while the latter leads to less EKE being produced by the mean flow due to eddy momentum fluxes.

In the A2 region, the M_{K_E} term is also larger than the D_{K_E} term, just like in the A1 region. However, it is the M_{K_E} and A_{K_E} terms that contribute to the seasonality of the EKE, not the D_{K_E} term. The M_{K_E} (A_{K_E}) is reduced from 5.3 (4.7) mW/m^2 during winter to 3.9 (0.8) mW/m^2 during summer. A comparison between the two experiments indicates that the M_{K_E} term dominates the change of the EKE budget in the A2 region. That is, the reduced horizontal velocity shear contributes the most to the EKE reduction. Because the velocity shear is always cyclonic in the A2 region (Fig. 2), the reduction in M_{K_E} leads to a reduction in the amplitudes of the CEs here. In winter, the eddy energy gained by D_{K_E}, M_{K_E} and A_{K_E} for ExpA is 0.7, 5.3 and 4.7 mW/m^2, respectively, but the values decrease to 0.5, 2.1 and 3.0 mW/m^2 for ExpB, approximately 29%, 60% and 36% of that in ExpA, respectively. In summer, D_{K_E} and M_{K_E} for ExpB decrease by more than 50%, while the A_{K_E} term increases by 75%, from 0.8 mW/m^2 in ExpA to 1.4 mW/m^2 in ExpB. In ExpB, the enhancement of A_{K_E} in summer is caused by the strong northeastward flow transporting EKE from the east coast of Vietnam, which is an active eddy region in this season.

In order to further analyze the change of eddy energy, we use the normalization composite analysis to eddies in DJF and JJA for the northern SCS. Figure 10 shows the normalization composite of D_{K_E} for CEs and AEs in the northern SCS. In winter, the D_{K_E} of CEs in ExpB is reduced from 1.5 mW/m^2 to 1.8 mW/m^2 in ExpA. However, for AEs, the D_{K_E} in ExpB is increased, from 1.2 mW/m^2 in ExpA to 4.8 mW/m^2 in ExpB. In summer, the D_{K_E} of CEs in ExpB is reduced from 1.9 mW/m^2 to 4.8 mW/m^2 in ExpA. The D_{K_E} of AEs in ExpB is also reduced from 0.4 mW/m^2 to 1.2 mW/m^2 in ExpA. Then Fig.11 shows the normalization composite of M_{K_E} for CEs and AEs in the northern SCS. For CEs in winter, the M_{K_E} of ExpB is reduced, from 6.2 mW/m^2 to 12.3 mW/m^2 in ExpA. And for AEs, the M_{K_E} of ExpB is reduced from 4.6 mW/m^2 to 9.9 mW/m^2 in ExpA. For CEs in summer, the M_{K_E} of ExpB is reduced, from 7.6 mW/m^2 to 10.7 mW/m^2 in ExpA. And for AEs,

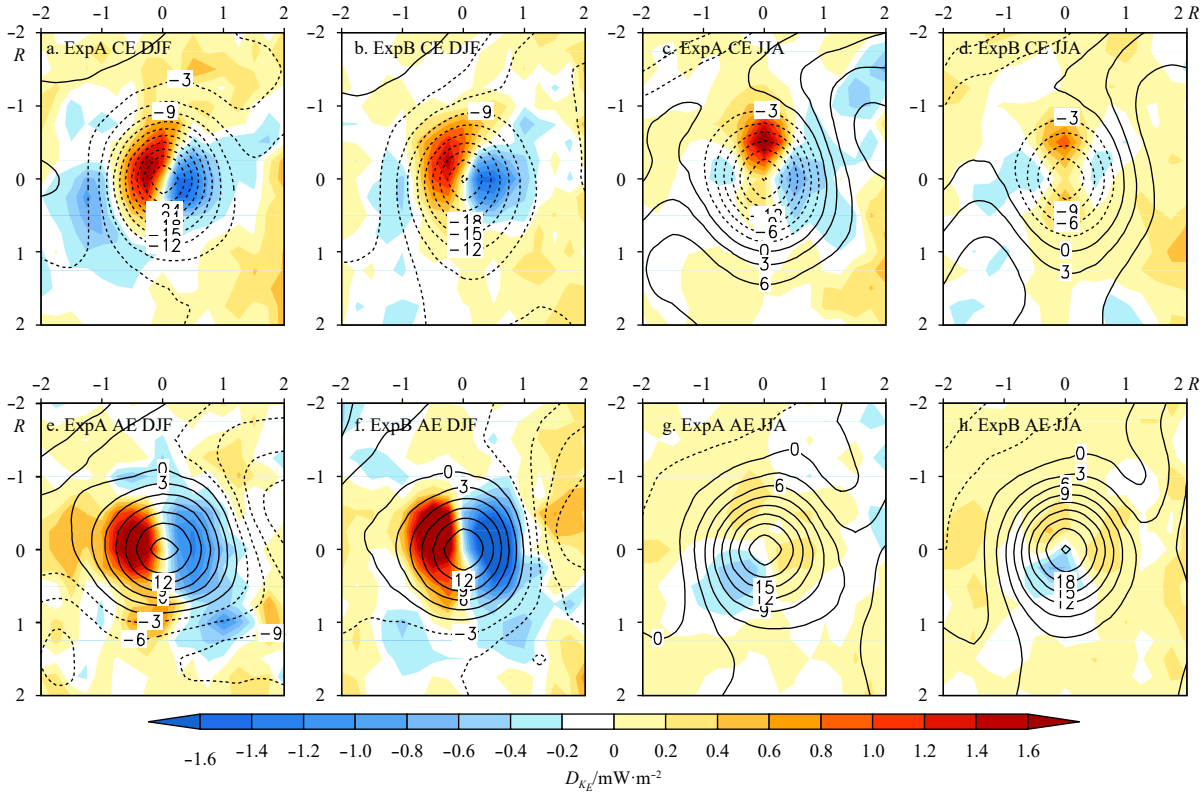

Fig. 10. The normalization composite of D_{K_E} (shaded, mW/m^2) and SSHA (contour, cm) in the northern SCS for CEs and AEs in winter (a, b, e, f) and summer (c, d, g, h). Number 1 and 2 refers to the one time and two times of radius and the letter *R* refers to the radius, respectively.

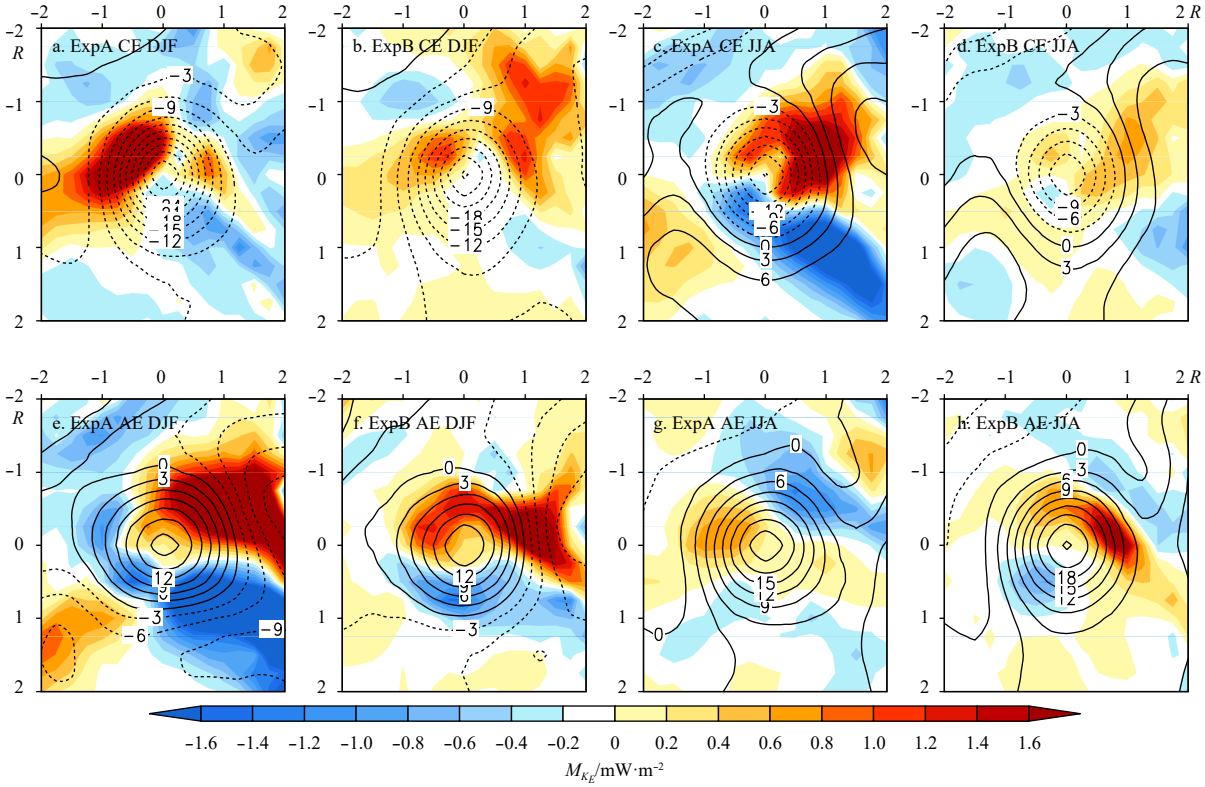

Fig. 11. The normalization composite of M_{K_E} (shaded, mW/m²) and SSHA (contour, cm) in the northern SCS for CEs and AEs in winter (a, b, e, f) and summer (c, d, g, h). The number 1 and 2 refers to the one time and two times of radius and the letter *R* refers to the radius, respectively.

however, the M_{K_E} of ExpB is increased from 9.8 mW/m² to 8.5 mW/m² in ExpA. The composite analysis confirms that the reduced eddy energy, especially D_{K_E} and M_{K_E}, leads to the decreased eddy number and amplitude in the northern SCS due to the optimization of KI. The abnormal increasing of D_{K_E} in winter and M_{K_E} in summer for AEs in ExpB results in the little amplitude increasing of AEs in the northern SCS. The normalization composite of A_{K_E} for CEs and AEs is also computed (not shown). The conclusions inferred from it is similar to that of D_{K_E} and M_{K_E}, that is there are also abnormal increasing in the eddy energy of AEs in the northern SCS. In addition, the normalization composite values of D_{K_E} and M_{K_E} in the northern SCS imply that the barotropic instability play the major role.

Based on the EKE budget analysis, we found that the changes in the D_{K_E} term also cannot be neglected, although it is not the dominating term. The decreases in D_{K_E} for ExpB are all more than approximately 30% for two regions. Because the geostrophic relationship is valid for both the large-scale currents and MEs, a reduction of the surface velocity is also associated with a reduction in the thermocline gradient and an increase in its stability. That tends to lead to less EAPE being transformed into EKE, and thus small values of D_{K_E}. Figure 12 shows the potential densities (shaded) and the zonal currents (contour) along 115°E (in the A2 region) for ExpA and ExpB. The thermocline ridge near 19°N for ExpA is greatly reduced in ExpB, which leads to a reduction in the geostrophic current and its shear in both seasons. This situation also occurs in the A1 region (not shown). We have also computed the pressure work terms, $-\nabla\cdot\left(\overrightarrow{u'p'}\right)$, for the two experiments. The spatial distribution is similar to the transport of EKE, but with a smaller magnitude (not shown).

6 Concluding remarks

In this study, the effect of the KI optimization on the simulation of MEs in the northern SCS was investigated by comparing two numerical experiments from an eddy-resolving ocean general circulation model. The main conclusions are as follows.

(1) The optimization of the KI does reduce the ME activities in the northern SCS. The EKEs in the studied domains, the A1 and A2 regions, are reduced by approximately 20%–40% in ExpB, in which the KI was significantly reduced by adding islands in the LS. That is, the bias in the modeled EKE was remarkably attenuated, which is a common problem in state-of-the-art eddy-resolving ocean models in the northern SCS.

(2) The number of CEs and AEs are both decreased in the northern SCS, but the decrease of AEs is more significant, at approximately 40% in the A1 and A2 regions. The amplitudes of the MEs are reduced by approximately 20% in ExpB, especially for the CEs. As a result, the generation number of AEs and the amplitude of CEs simulated by ExpB is more similar to that observed in satellite compared with ExpA after optimizing the KI. The optimization of the KI can improve the simulation of MEs in the northern SCS, although there are still discrepanicies in ExpB compared with the observations. However, other properties that are not related to the amplitude, such the radius, the lifetime and the moving speed, do not change much.

(3) The three terms of the EKE budget were investigated are D_{K_E}, M_{K_E} and A_{K_E}. These represent the changes of EKE due to the EAPE, the eddy momentum fluxes, and the energy transported by both the mean and eddy flow, respectively. All three terms con-

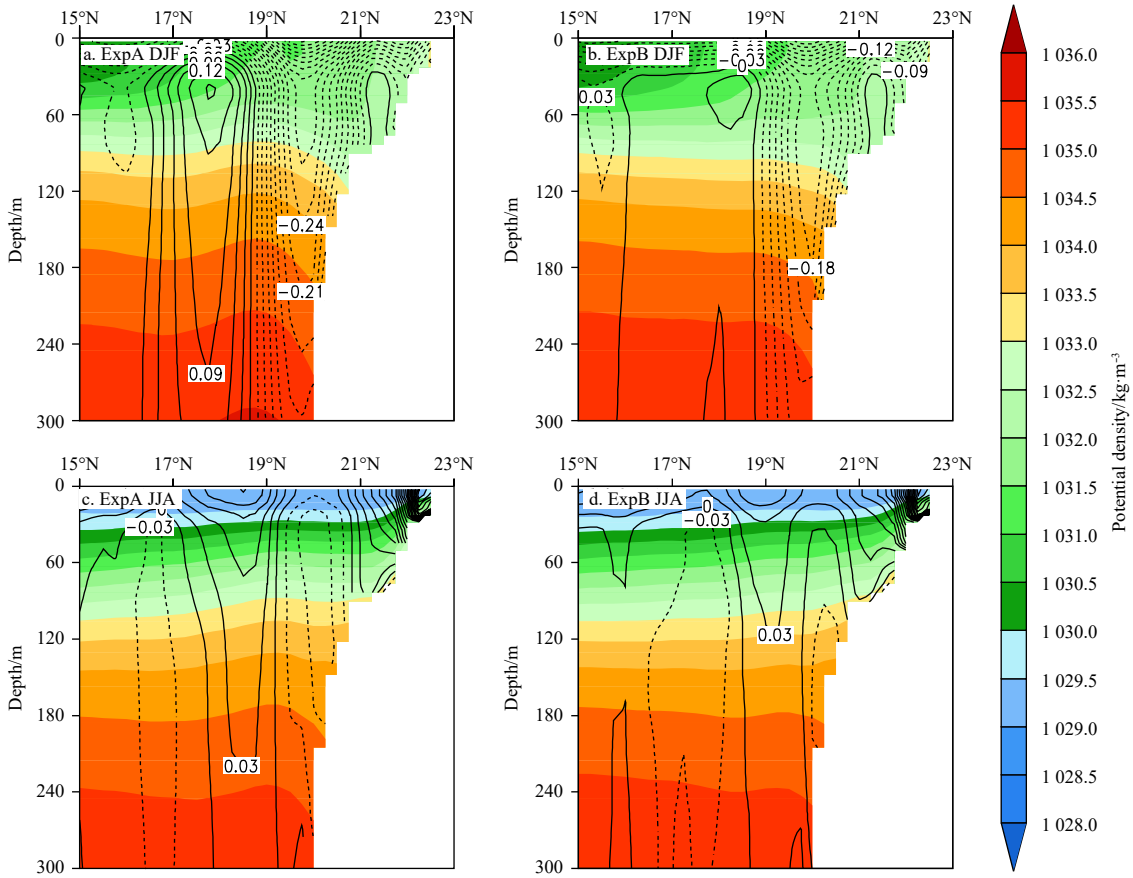

Fig. 12. The potential densities (shaded, kg/m^3) and zonal current speed (contour, m/s) along the 115°E for ExpA in DJF (a) and JJA seasons (c). (b, d) is the same as (a, c), but for ExpB.

tribute to the decrease in EKE simulated by ExpB, but different terms dominate the budget in different regions and seasons: in the A1 region A_{K_E} dominates the budget in winter, while M_{K_E} and A_{K_E} dominate in summer; in the A2 region, the M_{K_E} term dominates the budget in both seasons.

(4) The normalization composite of eddies shows that increasing of D_{K_E} in winter and M_{K_E} in summer for AEs may lead to the little increasing of AE amplitude in the northern SCS.

In summary, there are three processes that the optimization of KI affects the MEs in the northern SCS. First, the KI may change the EKE through directly transporting EKE into the northern SCS. This mechanism is mainly evident in the A1 region during winter, when the KI is strongest. Second, the KI may affect surface currents and further change the EKE through barotropic instabilities due to changes in the horizontal velocity shear in the northern SCS. This mechanism is the most important process in the A2 region and also dominates the EKE budget in the A1 region during summer. Third, changes in the surface currents caused by the KI may also cause changes in the thermocline slope. This third mechanism is not the dominant process of the changes between the two experiments, but the baroclinic instability still plays an important role in the EKE budget for both of the regions in this study.

As shown above, the simulated EKE in the northern SCS is significantly reduced in ExpB; however, it is still much larger than that seen in the satellite data. In addition to the KI, there are still several possible candidates for the overestimation of the EKE in the eddy-resolving models: the underestimation of the energy dissipation due to the subgrid parameterization and the lack of the air-sea feedbacks in the stand-alone ocean model forced by the prescribed atmospheric datasets, and others. The effects of these processes on the simulation of the MEs need to be investigated further.

Acknowledgements

The satellite data used in this paper are from AVISO (http://www.aviso.oceanobs.com/). The model data are from LICOM2.0.

References

Chaigneau A, Eldin G, Dewitte B. 2009. Eddy activity in the four major upwelling systems from satellite altimetry (1992–2007). Progress in Oceanography, 83(1–4): 117–123

Chelton D B, Schlax M G, Samelson R M. 2011. Global observations of nonlinear mesoscale eddies. Progress in Oceanography, 91(2): 167–216, doi: 10.1016/j.pocean.2011.01.002

Chen Gengxin, Hou Yijun, Chu Xiaoqing. 2011. Mesoscale eddies in the South China Sea: mean properties, spatiotemporal variability, and impact on thermohaline structure. Journal of Geophysical Research: Oceans, 116(C6): C06018

Chen Gengxin, Gan Jianping, Xie Qiang, et al. 2012. Eddy heat and salt transports in the South China Sea and their seasonal modulation. Journal of Geophysical Research: Oceans, 117(C5): C05021, doi: 10.1029/2011JC007724

Chen Ru, Flierl G R, Wunsch C. 2014. A description of local and nonlocal eddy-mean flow interaction in a global eddy-permitting state estimate. Journal of Physical Oceanography, 44(9): 2336–2352, doi: 10.1175/JPO-D-14-0009.1

Chen Gengxin, Wang Dongxiao, Dong Changming, et al. 2015. Observed deep energetic eddies by seamount wake. Scientific Reports, 5: 17416, doi: 10.1038/srep17416

Chu Xiaoqiang, Dong Changming, Qi Yiquan. 2017. The influence of ENSO on an oceanic eddy pair in the South China Sea. Journal of Geophysical Research: Oceans, 122(3): 1643–1652, doi: 10.1002/2016JC012642

Chu P C, Fan Chenwu, Lozano C J, et al. 1998. An airborne expendable bathythermograph survey of the South China Sea, May 1995. Journal of Geophysical Research: Oceans, 103(C10): 21637–21652, doi: 10.1029/98JC02096

Ducet N, Le Traon P Y, Reverdin G. 2000. Global high-resolution mapping of ocean circulation from TOPEX/Poseidon and ERS-1 and -2. Journal of Geophysical Research: Oceans, 105(C8): 19477–19498, doi: 10.1029/2000JC900063

Feng Baoxin, Liu Hailong, Lin Pengfei, et al. 2017. Meso-scale eddy in the South China Sea simulated by an eddy-resolving ocean model. Acta Oceanologica Sinica, 36(5): 9–25, doi: 10.1007/s13131-017-1058-3

Gent P R, McWilliams J C. 1990. Isopycnal mixing in ocean circulation models. Journal of Physical Oceanography, 20(1): 150–155, doi: 10.1175/1520-0485(1990)020<0150:IMIOCM>2.0.CO;2

He Yinghui, Cai Shuqun, Wang Dongxiao, et al. 2015. A model study of Luzon cold eddies in the northern South China Sea. Deep Sea Research Part I: Oceanographic Research Papers, 97: 107–123, doi: 10.1016/j.dsr.2014.12.007

Huang Zhida, Liu Hailong, Lin Pengfei, et al. 2017. Influence of island chains on the Kuroshio intrusion in the Luzon Strait. Advances in Atmospheric Sciences, 34(3): 397–410, doi: 10.1007/s00376-016-6159-y

Isern-Fontanet J, García-Ladona E, Font J. 2003. Identification of marine eddies from altimetric maps. Journal of Atmospheric and Oceanic Technology, 20(5): 772–778, doi: 10.1175/1520-0426(2003)20<772:IOMEFA>2.0.CO;2

Isern-Fontanet J, García-Ladona E, Font J. 2006. Vortices of the Mediterranean Sea: an altimetric perspective. Journal of Physical Oceanography, 36(1): 87–103, doi: 10.1175/JPO2826.1

Jia Yinglai, Liu Qinyu. 2004. Eddy shedding from the Kuroshio bend at Luzon Strait. Journal of Oceanography, 60(6): 1063–1069, doi: 10.1007/s10872-005-0014-6

Jia Yinglai, Chassignet E P. 2011. Seasonal variation of eddy shedding from the Kuroshio intrusion in the Luzon strait. Journal of Oceanography, 67(5): 601–611, doi: 10.1007/s10872-011-0060-1

Large W G, Yeager S G. 2004. Diurnal to decadal global forcing for ocean and sea-ice models: The data sets and flux climatologies. NCAR Technical Note NCAR/TN-460+STR, National Center for Atmospheric Research, Boulder, Colorado

Li Li, Nowlin W D Jr, Su Jilan. 1998. Anticyclonic rings from the Kuroshio in the South China Sea. Deep Sea Research Part I: Oceanographic Research Papers, 45(9): 1469–1482, doi: 10.1016/S0967-0637(98)00026-0

Lin Pengfei, Wang Fan, Chen Yongli, et al. 2007. Temporal and spatial variation characteristics on eddies in the South China Sea I. *statistical analyses*. Haiyang Xuebao (in Chinese), 29(3): 14–22

Lin Xiayan, Dong Changming, Chen Dake, et al. 2015. Three-dimensional properties of mesoscale eddies in the South China Sea based on eddy-resolving model output. Deep Sea Research Part I: Oceanographic Research Papers, 99: 46–64, doi: 10.1016/j.dsr.2015.01.007

Liu Qinyu, Kaneko A, Su Jilan. 2008. Recent progress in studies of the South China Sea circulation. Journal of Oceanography, 64(5): 753–762, doi: 10.1007/s10872-008-0063-8

Liu Hailong, Lin Pengfei, Yu Yongqiang, et al. 2012. The baseline evaluation of LASG/IAP climate system ocean model (LICOM) version 2. Acta Meteorologica Sinica, 26(3): 318–329, doi: 10.1007/s13351-012-0305-y

Metzger E J, Hurlburt H E. 2001. The nondeterministic nature of Kuroshio penetration and eddy shedding in the South China Sea. Journal of Physical Oceanography, 31(7): 1712–1732, doi: 10.1175/1520-0485(2001)031<1712:TNNOKP>2.0.CO;2

Nan Feng, Xue Huijie, Xiu Peng, et al. 2011. Oceanic eddy formation and propagation southwest of Taiwan. Journal of Geophysical Research: Oceans, 116(C12): C12045, doi: 10.1029/2011JC007386

Pullen J, Doyle J D, May P, et al. 2008. Monsoon surges trigger oceanic eddy formation and propagation in the lee of the Philippine islands. Geophysical Research Letters, 35(7): L07604

Qu Tangdong. 2000. Upper-layer circulation in the South China Sea. Journal of Physical Oceanography, 30(6): 1450–1460, doi: 10.1175/1520-0485(2000)030<1450:ULCITS>2.0.CO;2

Roeske F. 2001. An atlas of surface flues based on the ECMWF re-analysis: A climatological dataset to force global ocean general circulation models. Report No. 323. Hamburg: Max-Planck-Institut fur Meteorologies , 31

Su Jilan, Xu Jianping, Cai Shuqun, et al. 1999. Gyres and Eddies in the South China Sea. Onset and Evolution of the South China Sea Monsoon and its Interaction with the Ocean (in Chinese). Beijing: Beijing Meteorological Press, 272–279

Sun Zhongbin, Zhang Zhiwei, Zhao Wei, et al. 2016. Interannual modulation of eddy kinetic energy in the northeastern South China Sea as revealed by an eddy-resolving OGCM. Journal of Geophysical Research: Oceans, 121(5): 3190–3201, doi: 10.1002/2015JC011497

Wang Liping, Koblinsky C J, Howden S. 2000. Mesoscale variability in the South China Sea from the Topex/Poseidon altimetry data. Deep Sea Research Part I: Oceanographic Research Papers, 47(4): 681–708, doi: 10.1016/S0967-0637(99)00068-0

Wang Guihua, Su Jilan, Chu P C. 2003. Mesoscale eddies in the South China Sea observed with altimeter data. Geophysical Research Letters, 30(21): 2121, doi: 10.1029/2003GL018532

Wang Chunzai, Wang Weiqiang, Wang Dongxiao, et al. 2006. Interannual variability of the South China Sea associated with El Niño. Journal of Geophysical Research: Oceans, 111(C3): C03023

Wang Guihua, Chen Dake, Su Jilan. 2008. Winter eddy genesis in the eastern South China Sea due to orographic wind jets. Journal of Physical Oceanography, 38(3): 726–732, doi: 10.1175/2007JPO3868.1

Wang Qiang, Zeng Lili, Zhou Weidong, et al. 2015. Mesoscale eddies cases study at Xisha waters in the South China Sea in 2009/2010. Journal of Geophysical Research: Oceans, 120(1): 517–532, doi: 10.1002/2014JC009814

Xiu Peng, Chai Fei, Shi Lei, et al. 2010. A census of eddy activities in the South China Sea During 1993–2007. Journal of Geophysical Research: Oceans, 115(C3): C03012

Yang Haiyuan, Wu Linxin, Liu Hailong, et al. 2013. Eddy energy sources and sinks in the South China Sea. Journal of Geophysical Research: Oceans, 118(9): 4716–4726, doi: 10.1002/jgrc.20343

Yu Yongqiang, Liu Hailong, Lin Pengfei. 2012. A quasi-global 1/10° eddy-resolving ocean general circulation model and its preliminary results. Chinese Science Bulletin, 57(30): 3908–3916, doi: 10.1007/s11434-012-5234-8

Yuan Dongliang, Han Weiqing, Hu Dunxin. 2006. Surface Kuroshio path in the Luzon Strait area derived from satellite remote sensing data. Journal of Geophysical Research: Oceans, 111(C11): C11007, doi: 10.1029/2005JC003412

Zhang Zhiwei, Zhao Wei, Tian Jiwei, et al. 2013. A mesoscale eddy pair southwest of Taiwan and its influence on deep circulation. Journal of Geophysical Research: Oceans, 118(12): 6479–6494, doi: 10.1002/2013JC008994

Zhang Zhiwei, Tian Jiwei, Qiu Bo, et al. 2016. Observed 3D structure, generation, and dissipation of oceanic mesoscale eddies in the South China Sea. Scientific Reports, 6: 24349, doi: 10.1038/srep24349

Zhang Zhiwei, Zhao Wei, Qiu Bo, et al. 2017. Anticyclonic eddy sheddings from Kuroshio Loop and the accompanying cyclonic eddy in the northeastern South China Sea. Journal of Physical Oceanography, 47(6): 1243–1259, doi: 10.1175/JPO-D-16-0185.1

Zhou Tianjun, Yu Yongqiang, Liu Yimin, et al. 2014. Flexible Global Ocean-Atmosphere-Land System Model. Berlin Heidelberg: Springer-Verlag

Zhuang Wei, Xie Shangping, Wang Dongxiao, et al. 2010. Intraseasonal Variability in Sea Surface Height Over the South China Sea. Journal of Geophysical Research: Oceans, 115(C4): C04010